Research Article Vol. 60, No. 4 / 1 February 2021 / Applied Optics 1021

applied optics

Instability mechanism and discharge regime diagnosis of microthrusters based on plasma properties

Fangyi Wang,[1,2] Shaohua Zhang,[2,*] Yan Liu,[2,3,4] and Xilong Yu[1,2]

[1]State Key Laboratory of High Temperature Gas Dynamics, Institute of Mechanics, Chinese Academy of Sciences, Beijing 100190, China
[2]School of Engineering Science, University of Chinese Academy of Sciences, Beijing 100049, China
[3]Key Laboratory of Advanced Energy and Power, Institute of Engineering Thermophysics, Chinese Academy of Sciences, Beijing 100190, China
[4]Research Center for Clean Energy and Power, Chinese Academy of Sciences, Lianyungang, Jiangsu 22046, China
*Corresponding author: shzh@imech.ac.cn

Received 10 November 2020; revised 30 December 2020; accepted 2 January 2021; posted 5 January 2021 (Doc. ID 414608); published 28 January 2021

In order to make it possible to control the plasma state and predict the regime transitions via coupling optical and electrical diagnosis in aerospace engineering, we have experimentally investigated the regime transitions under 0.1–15 kPa with an input discharge power of 0–25 W in a parallel-plate electrode configuration. An abnormal glow discharge (AGD), filamentary discharge (FD), and arc discharge (AD) are distinguished using the voltage–current characteristics under different gas pressures. The electron excitation temperature (T_e), electron density (N_e), spatial resolutions of T_e and N_e, and ionization degree are obtained via optical emission spectroscopy to reveal the transition mechanisms. Thermal instability, characterized by T_e, plays a dominant role during the transition from an AGD to an FD. The conclusions are supported by analysis of ionization degree, whereas electronic instability becomes the dominant mechanism in the transition from an FD to an AD. This is related to collision kinetics because of an observed drop in N_e, which is verified by the spatial resolution as well. Moreover, planar laser-induced fluorescence provides further insight into the instantaneous location and relative number variation of Ar $1s_5$ metastable atoms, which agrees well with the plasma properties mentioned above. In addition, a pressure of 1 kPa with a maximum input power of 17.5 W are specified as suitable working parameters for further study when applied to microthrusters due to its higher N_e and better stability.

https://doi.org/10.1364/AO.414608

1. INTRODUCTION

Gas discharge plasma has been the subject of much research, owing to the large chemical freedom offered by its nonequilibrium aspects. Many fields, such as surface etching and modification, prefer to use stable and dispersed plasma in a large area with good repeatability [1–6], which is most commonly produced by a glow discharge (GD). Hence, the GD has aroused more interest than other discharge types and has been applied more broadly over the past decades. However, it is difficult to maintain a stable GD in practical aerospace applications such as avionics propulsion or plasma-enhanced combustion of chemical thrusters [7–11]. Even tiny variations of the amplitude or repetition frequency of the applied voltage, or subtle changes of electrode surfaces and gas flow, could lead to a transition from a GD to a filamentary discharge (FD) and finally to an arc discharge (AD) or spark discharge. This is in addition to pressure oscillation in the cabin and an unsteady component environment. Regime transitions bring about many consequences: breakdown, device burnout, and other irreparable damage.

Unfortunately, currently available information is not quite sufficient for proper choice of the discharge parameters in application. Therefore, it is necessary to study the characteristics and mechanisms of regime transitions in discharges via real-time monitoring under conditions similar to those of aero-propulsion to comprehend the discharge performance and predict regime transition in advance. Passive feedback thereby turns into proactive macroregulation; that is, actively controlling the performance or efficiency of plasma enhancement.

Studies rarely involve external control of regime transitions. There is still no systematic theory of regime transitions because the chemical reactions in the plasma are complicated. In an earlier work, Fu *et al.* [12] demonstrated that transition processes of hollow cathode discharges at 0.06–50 kPa could be determined from the distribution of plasma properties based on numerical simulation. Pai *et al.* [13] demonstrated with optical diagnostics that the glow-to-spark transition is determined by thermal instability, but they did not observe any FD. Other

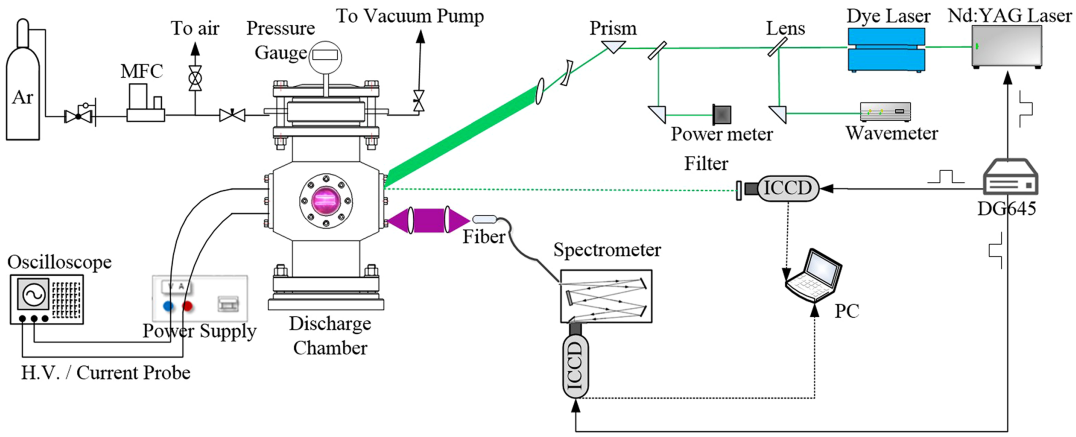

Fig. 1. Schematic of experimental setup.

work by Baeva *et al.* [14] focused more on the effects of electron transport properties on the transition from a normal glow to an AD at atmospheric pressure, which was not applicable to space environments. In addition, Borisyuk *et al.* [15] studied spatial–temporal evolution and plasma parameters for transitions in an abnormal glow discharge (AGD), but needle electrodes were unable to produce plasma with a large area. Elissev *et al.* [16] showed that cathode heating was the reason for transition, while some researchers [17,18] aimed at regime transition in low-temperature plasma produced by dielectric barrier discharge with an insulation layer that is unable to withstand the scorching temperature of aerospace propulsion. Most of this research, as others [19–26], lacked experiments to monitor discharge parameters or control regimes that apply to aerospace environments. Besides, research [27] shows that discharge mechanisms are easily affected by modified external parameters such as chemical input, pressure, and discharge configuration. This means that the comprehensive investigation and real-time diagnosis for regime transitions of specific discharges must be carried out, especially in environment of aero-propulsion so as to achieve external control of regime transitions or plasma enhancement.

Therefore, an input power of 0–25 W and typical gas pressure of 0.1–15 kPa are selected to study the vital plasma parameters via coupling optical and electrical diagnosis, for the purpose of controlling the plasma state and predicting the regime transitions in aerospace engineering. Voltage–current characteristics (VCCs) are applied to define the discharge regime, while quantitative data about plasma properties are measured by optical emission spectroscopy (OES). Meanwhile, metastable Ar atoms (Ar^M) are assessed by planar laser-induced fluorescence (PLIF). The dominant instability mechanisms of each transition and optimal settings for a microthruster are discussed based on the parameters mentioned above.

2. EXPERIMENTAL SETUP

A. Discharge Chamber

Figure 1 shows the schematic of the experimental setup in this work. Pure argon (99.999%) was introduced into the discharge chamber with a constant flow rate of 0.2 L/min and

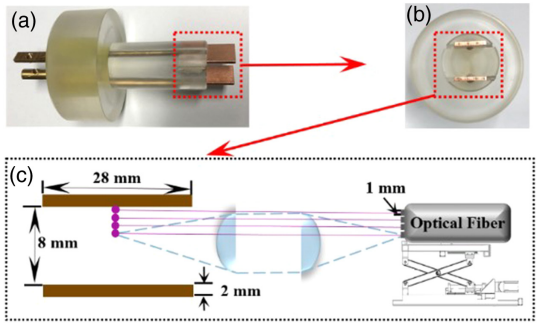

Fig. 2. Photographs of electrodes from (a) side and (b) front, and (c) position calibration system of OES diagnostics.

monitored by a mass flow controller. A stable chamber pressure and dynamic balance of argon gas were achieved through precise adjustment of the gas input and evacuation during the experiment. Parallel copper plates were used as electrodes; their surfaces were polished with fine-grained sandpaper, giving a roughness of about 1 μm. Electrodes were mounted on an insulating PMMA holder that positioned the electrodes at the center of the discharge chamber, as shown in Figs. 2(a) and 2(b). Cooling time was set as 10 min to ensure the same conditions of PMMA holder in each test; an infrared thermometer was also used to monitor temperature of the holder. The lower plates served as the anode with a high-voltage input while the upper plate was grounded. Supporting the discharge was an AC power supply (Coronalab CTP-2000 K, Nanjing, CN), whose phase was modulated with a signal generator (Agilent 33500B Series Waveform Generator, KEYSIGHT). The frequency of the applied voltage was maintained at 5 kHz. The real-time input voltage and current were monitored and recorded by probes (Rigol RP5600A 10:1 probe 600 MHz) with 1 MΩ and a 6–16 pF termination to an oscilloscope (Rigol DS6064 Digital Oscilloscope 4 channel 600 MHz 5 GSa/s).

B. OES Diagnostics

OES measurements were carried out with a fiber-based spectrometer (Spectrapro HRS-500, Princeton Instruments). An optical fiber was positioned on a displacement platform at the outer surface of a side optical window, which was made of fused

Table 1. Ar-I PLIF Schemes Examined in the Experiments

Transition Scheme (Paschen)	Transition Scheme(Racah)	λ_{12} (nm)[a]	λ_{23} (nm)	$A_{21}(s^{-1})$	$A_{23}(s^{-1})$
$1s_5 \rightarrow 2p_2 \rightarrow 1s_4$	$4s(^2P^0_{3/2})_2 - 4p'(^2P^0_{1/2})_1 - 4s(^2P^0_{3/2})_1$	696.7352	727.4940	6.39×10^6	1.83×10^6

[a]λ_{12} indicates absorption wavelength and λ_{23} indicates fluorescence wavelength (both are vacuum wavelengths). A_{21} and A_{23} are the spontaneous emission coefficients associated with each transition.

quartz. To compensate for the divergence angle of the fiber, a system based on plano–convex lenses was designed, as shown in Fig. 2(c). The exact location of the measuring point was obtained with a standard point source produced by a laser beam.

The optical signal was collected through the fiber into the spectrometer, whose entrance slit was set at 30 μm. The wavelength of the lighting system was calibrated with an Hg and N_e/Ar light source (IntelliCal, Princeton Instruments), and the intensity of the lighting was calibrated with a halogen lamp (Model 63355, Newport). The instrumental broadening was also obtained with a standard light source. The radiation was dispersed on a 1200 g/mm gating and detected by an intensified charge coupled deviceI (ICCD) (PI-MAX 4, Princeton Instruments). Considering the discharge frequency, the delay of the ICCD detector within OES experiment was fixed at 200 ns with a 200 μs exposed gate width.

C. PLIF Diagnostic

The metastable state of argon (Ar^M) was measured *in situ* via PLIF [28–30]. Ar^M was excited by a dye laser (Precisionscan, Sirah), which was pumped by an Nd:YAG laser (Quanta-Ray Pro250, Spectra-Physics) at 532 nm, which had a pulse width of 8 to 10 ns and a repetition rate of 10 Hz. The stable wavelength range of the dye laser is 667–720 nm, with maximum output at approximately 692 nm by Pyridine 1 dye dissolved in ethanol. In this work, $1s_5$ was selected because this state has the lowest excited energy. This state was pumped to upper state $2p_2$ optically at a rest wavelength of 696.7352 nm, which was selected as the excitation wavelength because it was a strong enough and comparatively well-isolated line [31]. Both the energies and transitions of excitation wavelength and fluorescence signal are listed in Table 1.

The wavelength and output power of the dye laser were monitored by wavelength meter and power meter, respectively. The excitation laser beam from the dye laser (~30 mJ/pulse) was turned into a laser sheet after passing a combination of a cylindrical lens and plano–convex lens. Through a slit aperture, the thickness and height of the laser sheet was limited to 1 and 25 mm, respectively. The measurement of Ar^M fluorescence intensity as a function of laser power was performed to confirm the laser energy within the linear excitation region. The fluorescence signal was captured by the other ICCD (PI-MAX 4, Princeton Instruments), which was perpendicular to the laser sheet. The positions of these devices are shown in Fig. 3. A narrowband filter (730 nm by 10 nm bandpass) was placed in front of the ICCD, which was used to separate the PLIF signal in 727.494 nm from the stray light and self-emissions of the plasma. To obtain a stronger signal intensity, the gate width of the ICCD was set at 200 ns, and the gain was 60 during the experiment. The synchronization sequence among the laser and ICCD cameras was achieved with a digital delay generator (Stanford, DG645).

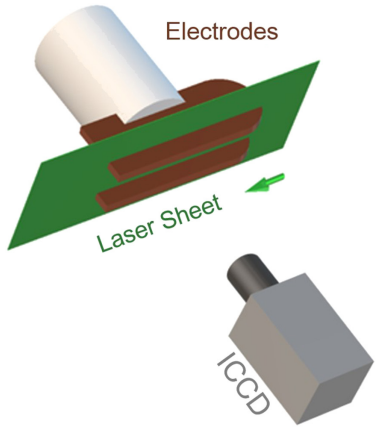

Fig. 3. PLIF setup.

3. RESULTS AND DISCUSSION

A. VCCs

The discharge phenomena are illustrated in Fig. 4, where the discharge regimes are distinguished easily from the position of luminescence. The AGD only covers the electrode surface, the FD consists of lines of discharge bridging the gap, and the AD is a thin arc cord. In addition, a clearer way to determine discharge regime is according to VCCs [32–36]. Figure 4 shows a series of input voltage–current (U–I) curves recorded on an oscilloscope. In the voltage–current curve in Fig. 4(a), the higher voltage and lower current can be identified as the GD regime. The peak current in the FD [Fig. 4(b)] gives information on the cathode spot with higher current density, which disappears in the AD [Fig. 4(c)]. There is a large current increase from the FD to the AD, accompanied by a sharp visual constriction in the discharge region.

The voltage and current amplitudes are provided in Fig. 5 to find out the individual function of each external parameter. The variation of the voltage with the mounting current indicates that the GD operates in an abnormal mode because the sustaining voltage increases in proportion to the current (as well as the input power), as seen in Fig. 5(a). Spot covers the whole surface of the cathode in AGD, and the number and energy of positive ions on the cathode are increased as voltage increases. In contrast, resistance of the discharge gas decreases sharply when the cathode reached a high temperature to produce a strong emission of hot electrons, which are defined as the transition to AD. Hence, the voltage applied in the FD [Fig. 5(b)] and AD [Fig. 5(c)] changes with current in an opposite way, which is called negative resistance. Comparing the fit curves from 2 and 5 kPa shows that the equivalent resistance of the plasma, which

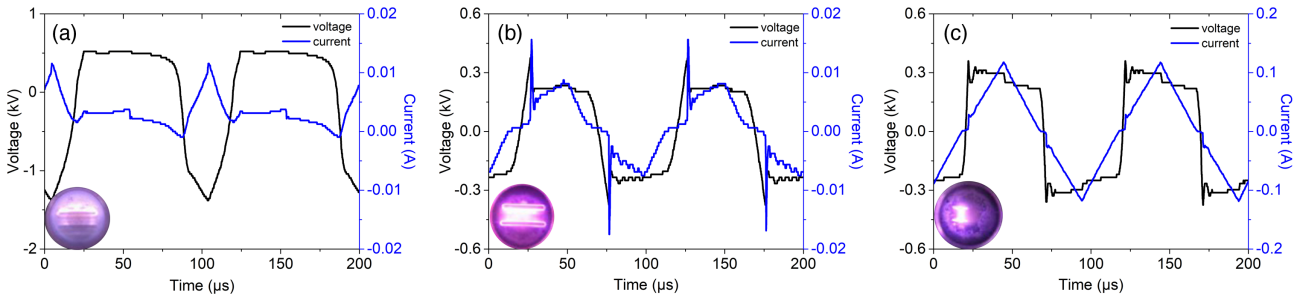

Fig. 4. U–I curves and discharge phenomena of (a) AGD, (b) FD, and (c) AD when $U = 0.8$ kV.

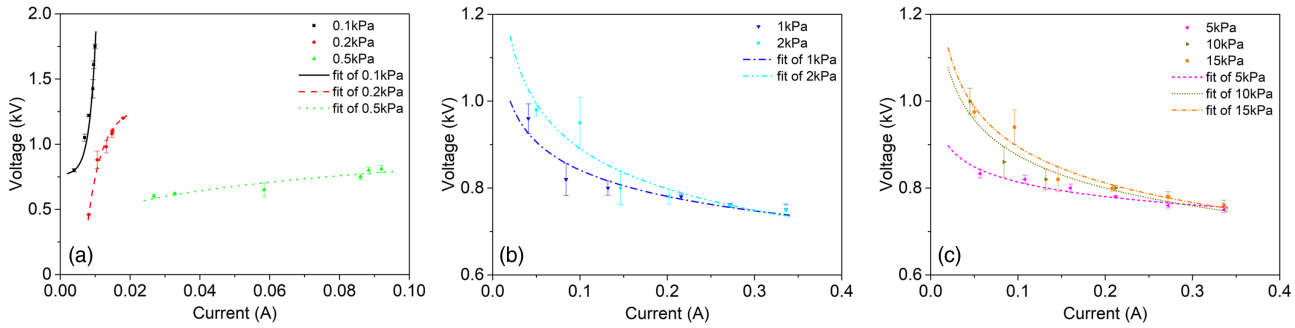

Fig. 5. Current and voltage amplitudes in (a) AGD, (b) FD, and (c) AD.

is the slope of the curve, decreases. Hence, the AGD, FD, and AD are certainly determined from either Fig. 4 or Fig. 5.

Moreover, internal mechanisms could be inferred on account of VCC [37,38]. Figure 5 implies two competing mechanisms, in that the same discharge power translates to lower current and higher voltage in the AGD but proceeds in an opposite direction in the FD and AD. The ionization rate is inferred in proportion to the mean free path and electron–neutral particle collision cross section. At low pressure [Fig. 5(a)], the effect of the collisions is greater, so the voltage needs to be decreased to maintain a stable current via a lower ionization rate. Apparently, the reduced mean free path has a major effect at higher pressure [Figs. 5(b) and 5(c)], which is compensated for with higher voltage. The conclusions are also demonstrated by T_e in the following.

B. Plasma Properties from Spectral Analysis

The spectral window for each test is from 200 to 900 nm during the whole experiment. Figure 6 only displays the spectral window where the emission spectral lines concentrate in an argon discharge. Obviously, the strong group of emission lines at 700–850 nm comes from the transition from the $3P^5 4P$ to the $3P^5 4S$ levels of Ar-I ($2P_n$ and $1s_n$ in the Paschen notation, respectively), while the weaker one in the range 400–500 nm is from the $5P \rightarrow 4S$ transitions of Ar-II. Moreover, both contain many lines, making the entire argon spectrum quite complex. Therefore, the major typical lines of atomic (Ar-I) and singly ionized (Ar-II) argon were chosen for studying plasma properties; their parameters are summarized in Table 2. In addition, to calculate plasma properties, it is necessary to correct the system response and subtract the baseline before fitting with a Voigt

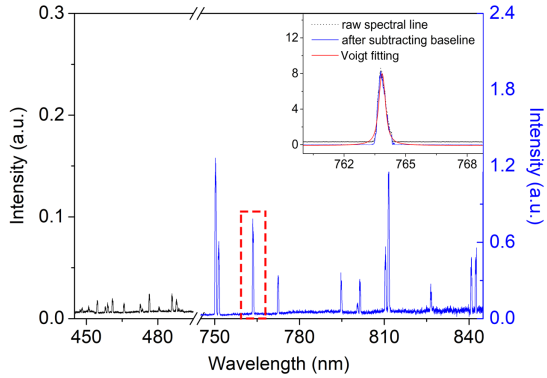

Fig. 6. Typical argon spectrum for $U = 0.8$ kV, $P = 200$ Pa, and process of Voigt fitting.

profile, as the inset shows in Fig. 6. Then the relative intensity of each spectral line can be obtained.

1. T_e

The T_e represents the part of the discharge energy emitted via radiative decay (>98.9%) [39] in a plasma. As a benchmark in the development of predictive models and simulations, the electron energy distribution function (EEDF), also characterized by T_e, matters a great deal in the dynamics of instabilities. This is provided that the plasma is in local thermodynamic equilibrium (LTE), i.e., the populations of argon atoms and ions at different energy levels follow a Boltzmann distribution. Hence, T_e can be determined via the equation

$$\ln\left(\frac{I\lambda}{A_{ki}g_k}\right) = -\frac{E_k}{kT_e} + C, \quad (1)$$

Table 2. Spectroscopic Data of Argon Lines Used in OES Diagnostics

Element	Wavelength λ (nm)	Absolute Spontaneous Transmission Probabilities $A_{ki}(10^6 s^{-1})$	Transition Energy of Upper Levels $E_k(cm^{-1})$	Statistical Weight g_k
Ar-I	696.5431	6.4	107496.4166	3
	706.7218	3.8	107289.7001	5
	763.5106	24.5	106237.5518	5
	772.4207	11.7	107496.4166	5
	811.5311	33	105462.7596	7
	842.4648	21.5	105617.2700	5
Ar-II	476.4864	64	160.239.4280	4
	480.6020	78	155043.1619	6

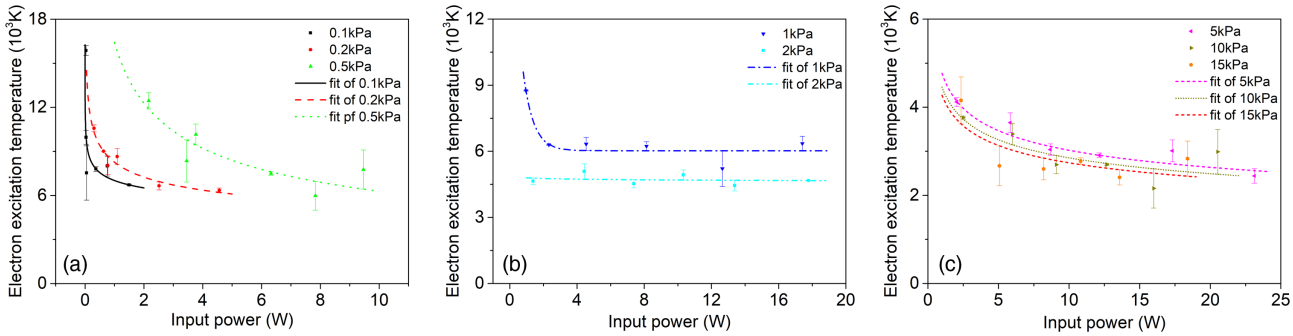

Fig. 7. T_e as a function of input power and gas pressure in (a) AGD, (b) FD, and (c) AD.

where I is the relative intensity of spectral lines, λ is the wavelength, k is Boltzmann's constant, g_k and E_k are the statistical weight and the energy of the upper level, respectively, and A_{ki} is the Einstein transition probability listed in Table 2. Six spectral lines of Ar-I in Table 2 are used to calculate T_e by Saha–Boltzmann method. Note that the mean fitting error of spectral lines intensity (that is, the area of each peak) is about 2.5%.

In Fig. 7, T_e drops with increasing input power, as illustrated when the gas pressure is constant. High-energy electrons gather around the surfaces of the electrodes in the AGD [Fig. 4(a)], so collision loss related to electrodes occurs constantly in the sheath in Fig. 7(a). The input power contributes to the following: a greater current density, which causes the electrode sheath to contract, thereby accelerating electron quenching; and a higher charged particle velocity because the voltage and edge effect increase. In contrast, the voltage reduction as input power rises [Figs. 5(b) and 7(c)] contributes to the FD and AD in Figs. 7(b) and 7(c). Electrons gain less energy in the same distance owing to the weaker electric field. As a result, the converse relationship between input power and electron energy coupling should be considered when adjusting parameters because the T_e intends to be constant as the power grows.

When the input power is kept constant, the T_e changes as the gas pressure increases, as illustrated in Fig. 7(a). In the AGD, the current changes as the gas pressure rises, as discussed in the last paragraph of the VCC section. This causes both the number and kinetic energy of positive ions that reach the cathode surface to increase. The high current also leads to more frequent collisions between electrons and neutral particles. This increase of energy consumption will be discussed in the next section. Although the voltage increases in the FD and AD under the same power, as illustrated in Figs. 7(b) and 7(c), the T_e diminishes with greater gas pressure. This is consistent with the explanation in VCC that the mean free path has a major impact at higher pressures.

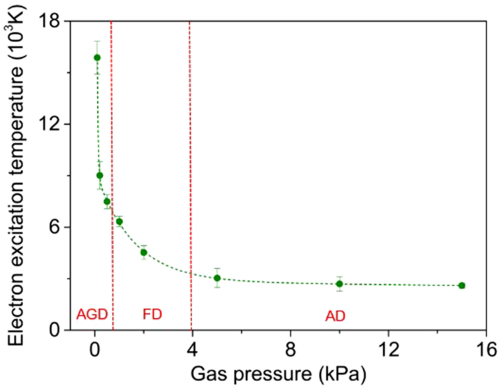

Fig. 8. T_e as a function of gas pressure when $U = 0.8$ kV.

Figure 8 shows the values of the T_e under different gas pressures while the voltage is fixed at 0.8 kV. Because the measuring pressure does not go below 100 Pa, there is no intense rise from zero in the T_e curves. The steeper gradient of the T_e in the transition from the AGD to the FD means more frequent collisions between electrons and neutral particles, which is consistent with the statement in VCC that this is the primary mechanism at lower pressure. Meanwhile, the decrease of the T_e in the AD is not as pronounced as in the FD because the discharge area is altered more in the FD, whereas the position of the thin arc cord is more stable in the AD. A dramatic variation of the T_e, as a perturbation, could initiate the thermal instability during

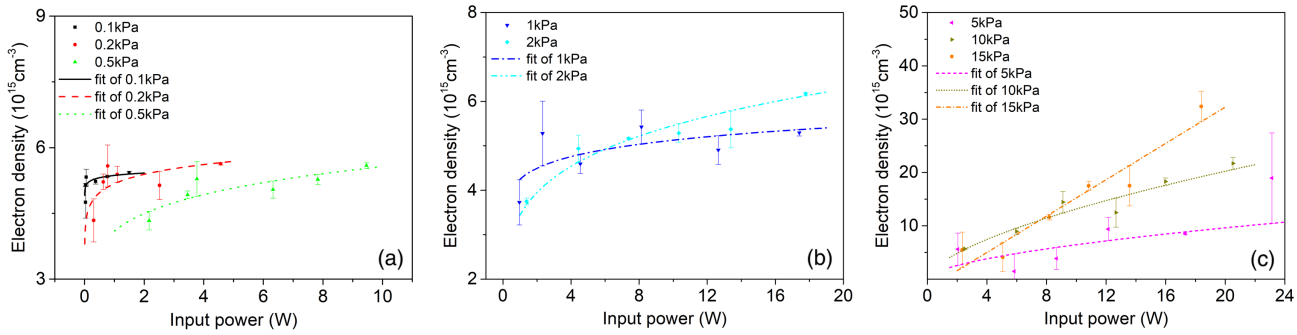

Fig. 9. N_e as a function of input power and gas pressure in (a) AGD, (b) FD, and (c) AD.

regime transitions, which is also evidenced by the following discussion of ionization degree.

2. Electron Number Density

Aside from the thermal effect, a chemical chain reaction is also accelerated by charged active particles with low activation energy produced by collisions between electrons and fuel molecules in space chemical propulsion. Consequently, the presence of even a small amount of free electrons may effectively improve combustion-assisted conditions. The value of full width at half-maximum (FWHM) of the chosen spectral lines could be obtained by function-fitting, as mentioned in the previous section. Instrument broadening, which is obtained from the standard Ne/Ar light source, van der Waals as well as natural broadening are removed to obtain stark broadening. Then, the electron density (N_e) is calculated from the following equation:

$$\Delta\lambda_{\text{stark}} = 2 \times [1 + 1.75 \times 10^{-4} N_e^{1/4} \alpha \times (1 - 0.068 N_e^{1/6} T_e^{-1/2})] \times 10^{-16} \omega N_e, \quad (2)$$

where α is the static ion-broadening parameter, and ω is the electron impact half-width [40]. So far, we are able to use the criterion $N_e \geq 1.4 \times 10^{14} T_e^{1/2} (\Delta E)^3$ from McWhirther's work [41] to check the LTE assumption.

In Fig. 9, the N_e shows a trend opposite to that of the T_e (Fig. 7) under different external parameters. Electron cooling means most kinetic energy of electrons has transferred to other electrons and converted to internal energy of neutral particles. The electron cooling here is accompanied by a decrease in the T_e and an increase in the N_e. In addition, the N_e can be estimated from the luminance of the discharge area. For instance, the brighter light-emitting layer in the AGD regime indicates higher N_e as the input power increases in Fig. 9(a); similar results are found in the work of Ivanavic *et al.* [42].

The N_e grows slowly from AGD to FD, as shown in Fig. 10. Before the stable plasma in the FD is disturbed, the electron production rate is equal to the quenching rate through the balance reached by various reactions. Figure 10 shows the abrupt drop of the N_e from the diffuse state (FD) to the constricted state (AD) with the formation of a thin cord of current and increasing current density. The fluctuations in the electric density seem to be initiated in the boundary regions and trigger some types of electronic instability, which supported by the discussion in

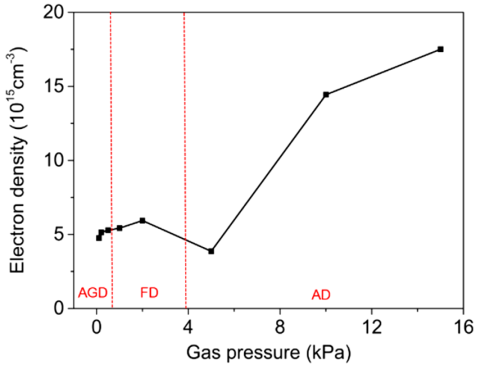

Fig. 10. N_e under different gas pressures when $U = 0.8$ kV.

Section 3.C, on spatial resolution. To give a clear analysis of discharge instabilities at the collisional level is quite complex and needs more elaborate information about production and loss mechanisms.

Furthermore, recent works have clearly shown that the main cause of constriction in argon at intermediate pressure (10^4–10^5 Pa) is the kinetic mechanism of the energy distribution, which inhomogeneous heating does not affect [43]. Owing to the finite volume of the discharge, constriction is caused by all changes of discharge regimes because they have an inherent spatial relationship. Hence, the spatial resolution is investigated later to verify this type of electronic instability.

3. Ionization Degree

The input power efficiency, characterized by the ionization degree (x), is quite useful for thrusters that have strict requirements for energy consumption and volume limitation. It is worth noting that the behavior of the ionization degree gives supplementary information to verify the leading role of the thermal effect in the transition from the AGD to the FD. As a significant quantitative index, the ionization degree is assessed by measuring the intensities of the spectral lines of atoms and ions.

The Saha equation under LTE conditions is

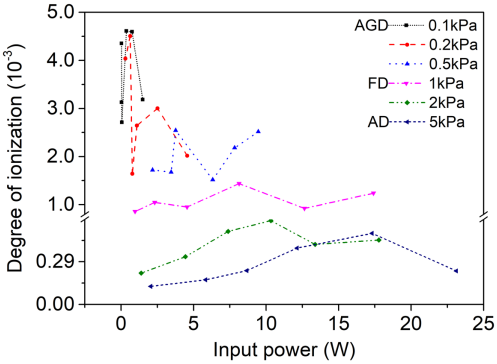

Fig. 11. Degree of ionization as a function of input power under different gas pressures.

$$\ln\frac{x_j}{1-x_j}=\ln\frac{I_{i,j}}{I_{a,j}}-\ln\frac{A_i g_i \lambda_a}{A_a g_a \lambda_i}+\ln\frac{Z_i}{Z_a}-\frac{5040}{T}(E_i-E_a), \tag{3}$$

where the subscript i stands for ions and a stands for atoms, and Z is the partition function given by

$$Z=\sum_{j=0}^{\infty} g_j \exp(-E_j/k_B T). \tag{4}$$

The effect of the input power on ionization degree has no particular law in Fig. 11. Only one curve of ionization degree in the AD regime is shown because there is little difference in each pressure case. Although the N_e increases along with input power in each regime, the ionization degree is not a monotonic function. Previous work [43] has found that thermal effect, which is characterized by the T_e, influences the ionization degree to some extent. This shows that the longitudinal oscillation of each pressure case, especially in the AGD regime, is mainly caused by the coupled interaction of the T_e and N_e, which has a trend opposite to input power. In addition, general ranges of ionization degree in three regimes are determined from Fig. 11. Under the same input power, the ionization degree basically decreases as the pressure rises.

A more obvious trend is shown in Fig. 12: that the ionization degree varies inversely with the gas pressure. This shows that the increase rate of the atomic density is higher than that of the N_e as pressure rises (Fig. 10). Furthermore, the ionization degree declines sharply during the transition from the AGD to the FD, which is primarily dominated by the T_e, shown in Fig. 8. To a certain degree, this verifies the leading role played by thermal instability in this transition. Nevertheless, there is no significant difference between the FD and AD; only a small decrease in AD is caused by contraction of the plasma region.

C. Spatial Resolution

1. Spatial Resolution of Plasma Properties

Electronic instability, which leads the transition from the FD to AD, influences the plasma properties according to collision kinetics. In what follows, we mainly compare the FD with the AD to test the reliability of the result. Spatially resolved spectra

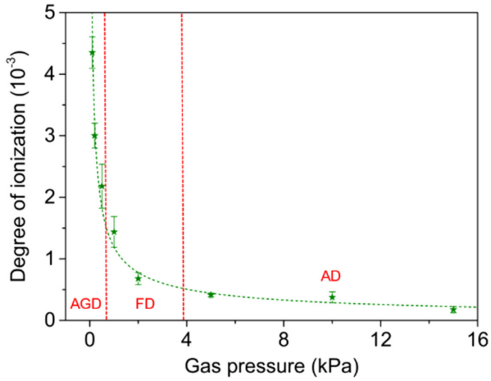

Fig. 12. Degree of ionization under different gas pressures when $U=0.8$ kV.

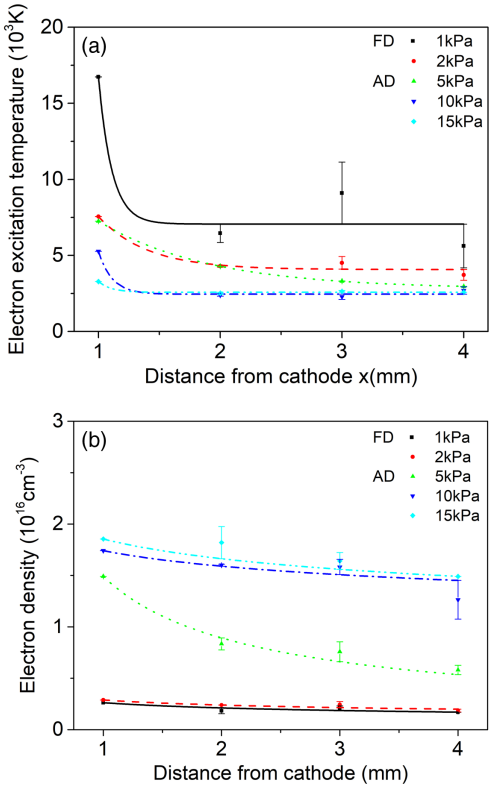

Fig. 13. (a) T_e and (b) N_e with spatial resolution when $U=0.8$ kV.

were obtained by measuring the emission light within 4 mm from the bottom surface of the cathode [Fig. 2(c)].

The T_e drops as a function of distance from the cathode in Fig. 13(a). The thickness of the cathode sheath is estimated to be of magnitude 10^1-10^2 μm because the range of the current density is 10^4-10^6 A/m^2. Both the diameter and distance of the nearest point to the cathode are 1 mm, which contains the plasma sheath area. The trend of T_e on the axis can be explained as follows. First, electrons absorb energy from the electric field of the sheath and induce secondary electrons emitted from the cathode surfaces. The weaker electric field and greater density of atoms causes electrons to collide more and consume more energy as they move further from the cathode.

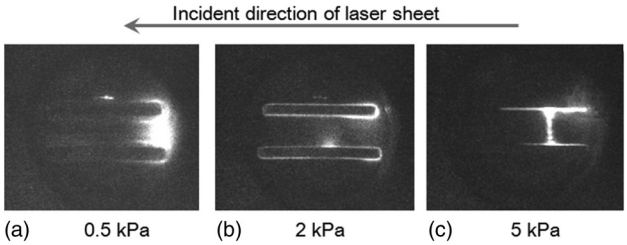

Fig. 14. Spatial distributions of metastable argon under different gas pressures in (a) AGD, (b) FD, and (c) AD.

In Fig. 13(b), the N_e on the axis from the FD to the AD increases on the whole. The maximum value occurs at the point closest to the cathode from 2 to 5 kPa, which proves that the N_e suddenly changes during the transition from the FD to the AD. This is probably caused by the electrons emitted at the cathode surface owing to field-enhanced thermo-emission after the contraction of the discharge area. The N_e soars in the sheath area, which means the plasma boundary develops runaway ionization or the ionization wave results in regime transition. This conclusion is reinforced by the similarities between these results and the identical behavior observed in DC microplasmas by Baeva *et al.* [44] and seen in other work [45].

2. Spatial Distribution of Ar^M

The EEDF is also determined by the excited state population and influences electronic instability. The information obtained via the PLIF supports the OES data; for example, some features of excitation of $2p$ atoms can be traced to the behavior of spectral lines. The PLIF of Ar^M (the excited population of $1s_5$ argon atoms) in the plasma region is shown in Fig. 3 to validate the foregoing discussions from a different point of view.

The photographs in Fig. 14 show the two-dimensional fluorescence signal of Ar^M, which demonstrates the spatial distributions of the Ar^M at various gas pressures. In the AGD regime of Fig. 15(a), the intensity of Ar^M fluorescence signal is higher on the side nearer to the laser sheet, perhaps owing to the scattered light of electrodes or target particles not excited with insufficient laser energy because of the strong laser absorption along the way. Qualitatively, the Ar^M relative number increases as pressure grows, which is reflected in the higher emission intensity of spectral lines with same upper $2p_2$ level in the OES spectra, such as line peaks at 772 and 826 nm. Increasing pressure leads to a decrease in direct ionization with respect to the step ionization, which raises the $1s_5$ relative number, as previous work [46] demonstrated through reaction rates of dominant kinetic processes. This also can be a reference for the current study of streamer-like instabilities in an AGD-type cathode region [47]. In Fig. 14(b), electrodes spots form, as we discussed for Fig. 4(b). The head of the electron avalanche and arc constriction are distinguished clearly in Fig. 14(c) on the basis of streamer theory.

Excited atom distribution is affected by the N_e and T_e when the discharge is in the LTE state. However, the effect of the T_e on the distribution is very small, since it is below 1.5 eV (Fig. 8) compared with N_e, whose range of variation can be several orders of magnitude larger in Fig. 10. Therefore, the gradient of the Ar^M relative number is greater in the first transition, from the AGD to the FD, as its line chart under different pressures is shown in Fig. 15. Representing the thermal instability, the T_e has a large variation while the N_e changes little. By contrast, the N_e increases by 1 order of magnitude of during the second transition, from the FD to the AD. However, the growth rate of the AD is obviously less than for the AGD and FD. Hence, the effect of the T_e seems more important during the first transition. The abrupt drop in Ar^M verifies the primary role of electronic instabilities in the transition from the FD to the AD. This is because the evolution in the electronic excited state population under different conditions can be a perturbation. The change in Ar^M, when coupled with a change in the electron energy distribution, leads to disorders in collision processes. This causes a positive feedback on the electronic instability and accelerates a transition from the relatively unstable diffuse mode to a much stabler AD.

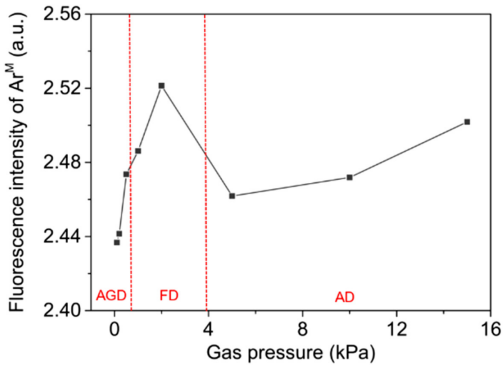

Fig. 15. Number of metastable Ar atoms ($1s_5$) among the three regimes when $U = 0.8$ kV.

4. CONCLUSIONS

In this work, both OES and PLIF were used to simultaneously determine plasma properties of specific parallel-plate copper electrodes within an argon discharge under a simulated environment of aero-propulsion. The results are listed in the following:

1. Discharge regimes of AGD, FD, and AD were distinguished based on the VCC as gas pressure increases from 0.1 to 15 kPa.
2. Sharper declines in both T_e and ionization degree are found from the AGD to the FD, which verified thermal instability plays a primary role in this transition.
3. Electronic instability becomes the dominant mechanism in the transition from the FD to the AD. This is related to collision kinetics, as shown by the abrupt drop observed in both N_e and number density of the $1s_5$ Ar^M. The dependence of the spatial resolution on this electronic instability was also discussed.
4. A pressure of 1 kPa with a maximum input power of 17.5 W is a more suitable working condition when applied to microthrusters as well as space engineering. This is because the FD has a larger effective discharge region, which prolongs the reaction time, and leads to higher N_e and better stability.

In summary, this study has provided fundamental data for online measurements in aerospace engineering, which is necessary for using external conditions to manage an optimal plasma state and predict regime transition.

Funding. National Natural Science Foundation of China (11672359, 11872368, 11927803); Natural Science Foundation of Beijing Municipality (BM2019001).

Acknowledgment. The authors acknowledge the technical assistance provided by D. H. Guo at the Institute of Mechanics, Chinese Academy of Sciences.

Disclosures. The authors declare no conflicts of interest.

REFERENCES

1. R. K. Marcus, *Glow Discharge Spectroscopies* (Springer, 2013).
2. J. R. Roth, D. M. Sherman, and S. P. Wilkinson, "Electrohydrodynamic flow control with a glow-discharge surface plasma," AIAA J. **38**, 1166–1172 (2000).
3. C. C. Farnell, C. C. Farnell, S. C. Farnell, and J. D. Williams, "Recommended practice for use of electrostatic analyzers in electric propulsion testing," J. Propul. Power **33**, 638–658 (2017).
4. S. B. Leonov and D. A. Yarantsev, "Near-surface electrical discharge in supersonic airflow: properties and flow control," J. Propul. Power **24**, 1168–1181 (2008).
5. C. Li and Y. Zhang, "Effect of glow discharge on hypersonic flat plate boundary layer," Appl. Math. Mech. **40**, 249–260 (2019).
6. T. Fukuyama and Y. Higashiura, "Study on dynamic behaviors of ionization waves influenced by feedback in a glow discharge plasma," Plasma Fusion Res. **13**, 3401073 (2018).
7. D. F. Zheng and B. Wang, "Utilization of nonthermal plasma in pulse detonation engine ignition," J. Propul. Power **34**, 539–549 (2018).
8. S. Marcuccio, M. Andrenucci, and A. Genovese, "Experimental performance of field emission microthrusters," J. Propul. Power **14**, 774–781 (1998).
9. Z. Wu, J. Xu, P. Chen, K. Xie, and N. Wang, "Maximum thrust of single dielectric barrier discharge thruster at low pressure," AIAA J. **56**, 2235–2241 (2018).
10. Y. Ding, H. Li, P. Li, B. Jia, L. Wei, H. Su, H. Sun, L. Wang, and D. Yu, "Effect of relative position between cathode and magnetic separatrix on the discharge characteristic of Hall thrusters," Vacuum **154**, 167–173 (2018).
11. L. Dorf, Y. Raitses, and N. J. Fisch, "Experimental studies of anode sheath phenomena in a Hall thruster discharge," J. Appl. Phys. **97**, 103309 (2005).
12. Y. Y. Fu, J. P. Verboncoeur, A. J. Christlieb, and X. X. Wang, "Transition characteristics of low-pressure discharges in a hollow cathode," Phys. Plasmas **24**, 7 (2017).
13. D. Z. Pai, D. A. Lacoste, and C. O. Laux, "Transitions between corona, glow, and spark regimes of nanosecond repetitively pulsed discharges in air at atmospheric pressure," J. Appl. Phys. **107**, 093303 (2010).
14. M. Baeva, D. Loffhagen, M. M. Becker, and D. Uhrlandt, "Fluid modelling of DC argon microplasmas: effects of the electron transport description," Plasma Chem. Plasma Process. **39**, 949–968 (2019).
15. Y. V. Borisyuk, N. M. Oreshnikova, D. V. Mozgrin, T. V. Stepanova, and A. A. Pisarev, "Pulse-periodic abnormal glow discharge in nitrogen, argon, hydrogen and their mixtures," J. Phys.: Conf. Ser. **747**, 012019 (2016).
16. S. I. Eliseev, A. A. Kudryavtsev, H. Liu, Z. Ning, D. Yu, and A. S. Chirtsov, "Transition from glow microdischarge to arc discharge with thermionic cathode in argon at atmospheric pressure," IEEE Trans. Plasma Sci. **44**, 2536–2544 (2016).
17. C. Meyer, S. Müller, B. Gilbert-Lopez, and J. Franzke, "Impact of homogeneous and filamentary discharge modes on the efficiency of dielectric barrier discharge ionization mass spectrometry," Anal. Bioanal. Chem. **405**, 4729–4735 (2013).
18. A. Belinger, N. Naudé, and N. Gherardi, "Transition from diffuse to self-organized discharge in a high frequency dielectric barrier discharge," Eur. Phys. J. Appl. Phys. **79**, 10802 (2017).
19. M. Fiebrandt, N. Bibinov, and P. Awakowicz, "Determination of atomic oxygen state densities in a double inductively coupled plasma using optical emission and absorption spectroscopy and probe measurements," Plasma Sources Sci. Technol. **29**, 045018 (2020).
20. N. Sahin, "An investigation of the spectral lines of argon discharge with low electron density," Optik **195**, 163165 (2019).
21. M. Slapanska, A. Hecimovic, J. T. Gudmundsson, J. Hnilica, W. Breilmann, P. Vasina, and A. von Keudell, "Study of the transition from self-organised to homogeneous plasma distribution in chromium HiPIMS discharge," J. Phys. D **53**, 155201 (2020).
22. G. D. Stancu, F. Kaddouri, D. A. Lacoste, and C. O. Laux, "Atmospheric pressure plasma diagnostics by OES, CRDS and TALIF," J. Phys. D **43**, 124002 (2010).
23. J. C. Nascimento, E. C. B. B. Aragão, A. D. Fernandes, F. T. F. Barbosa, L. M. S. Costa, D. C. Sousa, C. Oliveira, G. J. P. Abreu, K. G. Grigorov, P. Getsov, R. S. Pessoa, V. W. Ribas, and B. N. Sismanoglu, "Optical measurements of an atmospheric pressure microplasma jet aiming surface treatment," Am. J. Condens. Matter Phys. **4**, 8–18 (2014).
24. V. H. B. Hrycak, M. Jasiński, J. Mizeraczyk, J. Mullen, and P. Bruggeman, "Temperature and NO density measurements by LIF and OES on an atmospheric pressure plasma jet," J. Phys. D **46**, 095201 (2013).
25. P. Bruggeman and R. Brandenburg, "Atmospheric pressure discharge filaments and microplasmas: physics, chemistry and diagnostics," J. Phys. D **46**, 464001 (2013).
26. Y. Lizhen, Z. Yuefei, C. Qiang, Z. Guangqiu, and G. Yuanjing, "Characterization of the discharge in array needle cathodes and applications," Phys. Procedia **18**, 2–8 (2011).
27. N. Nafarizal, N. Takada, and K. Sasaki, "Production of Ar metastable atoms in the late afterglow of pulse-modulated RF magnetron sputtering plasmas," J. Phys. D **41**, 035206 (2008).
28. A. K. Hansen, M. Galante, D. McCarren, S. Sears, and E. E. Scime, "Simultaneous two-dimensional laser-induced-fluorescence measurements of argon ions," Rev. Sci. Instrum. **81**, 10D701 (2010).
29. Z. D. Short, M. U. Siddiqui, M. F. Henriquez, J. S. McKee, and E. E. Scime, "A novel laser-induced fluorescence scheme for Ar-I in a plasma," Rev. Sci. Instrum. **87**, 013505 (2016).
30. R. F. Kelly, "*Density and velocity measurement of ArI and ArII using laser induced fluorescence (LIF) in a large-scale helicon plasma*" (Ph.D. dissertation, University of New Mexico, 2018).
31. D. S. Thompson, T. E. Steinberger, A. M. Keesee, and E. E. Scime, "Laser induced fluorescence of Ar-I metastables in the presence of a magnetic field," Plasma Sources Sci. Technol. **27**, 065007 (2018).
32. Y. Guan, S. Wang, S. Tang, H. Mu, and Q. Liu, "Effect of power parameters on micro-discharge induced by corona discharge," Plasma Sci. Technol. **21**, 054007 (2019).
33. S. I. Al-Mayman, M. S. Al-Johani, K. O. Borisevich, A. A. Al-Musa, N. M. Al-Abbadi, A. V. Krauklis, and P. G. Stanovoi, "Syngas production in methane decomposition in the plasma of atmospheric pressure high-voltage discharge," Heat Transfer Res. **49**, 1119–1129 (2018).
34. R. Guan, Z. Jia, S. Fan, and Y. Deng, "Performance and characteristics of a small-current DC arc in a short air gap," IEEE Trans. Plasma Sci. **47**, 746–753 (2019).
35. Y. V. Borisyuk, V. V. Kozlova, D. V. Mozgrin, P. S. Nenashev, N. M. Oreshnikova, M. M. Berdnikova, and A. A. Pisarev, "Pulsed abnormal glow discharge with hollow cathode for nitriding of internal cylindrical surfaces," J. Phys. Conf. Ser. **941**, 012036 (2017).
36. A. I. Saifutdinov, I. I. Fairushin, and N. F. Kashapov, "Analysis of various scenarios of the behavior of voltage–current characteristics of direct-current microdischarges at atmospheric pressure," JETP Lett. **104**, 180–185 (2016).
37. C. Niu, S. Qin, X. Zhang, H. Zhao, X. Liu, H. Mu, and G. Zhang, "Discharge characteristics of argon atmosphere dielectric barrier with different *pd* values," in *12th International Conference on the Properties and Applications of Dielectric Materials (ICPADM)* (2018), pp. 856–862.
38. D. Marić, G. Malović, and Z. L. Petrović, "Space–time development of low-pressure gas breakdown," Plasma Sources Sci. Technol. **18**, 034009 (2009).

39. D. L. Crintea, U. Czarnetzki, S. Iordanova, I. Koleva, and D. Luggenholscher, "Plasma diagnostics by optical emission spectroscopy on argon and comparison with Thomson scattering," J. Phys. D **42**, 045208 (2009).
40. H. R. Griem, *Plasma Spectroscopy* (McGraw-Hill, 1961).
41. R. H. Huddlestone and S. L. Leonard, "Plasma diagnostic techniques," in *Plasma Diagnostic Techniques* (Academic, 1965), p. 206.
42. N. V. Ivanovic, "The study of Ar I and Ne I spectral line shapes in the cathode sheath region of an abnormal glow discharge," Atoms **7**, 9 (2019).
43. Y. B. Golubovskii, A. V. Siasko, and V. O. Nekuchaev, "Peculiarities of glow discharge constriction in helium," Plasma Sources Sci. Technol. **29**, 065020 (2020).
44. D. Fang and R. K. Marcus, "Use of a cylindrical Langmuir probe for the characterization of charged-particle populations in a planar, diode glow-discharge device," Spectrochim. Acta B Atom. Spectros. **45**, 1053–1074 (1990).
45. A. Khrabry, I. D. Kaganovich, V. Nemchinsky, and A. Khodak, "Investigation of the short argon arc with hot anode. I. Numerical simulations of non-equilibrium effects in the near-electrode regions," Phys. Plasmas **25**, 16 (2018).
46. X. M. Zhu, Y. K. Pu, N. Balcon, and R. Boswell, "Measurement of the electron density in atmospheric-pressure low-temperature argon discharges by line-ratio method of optical emission spectroscopy," J. Phys. D **42**, 5 (2009).
47. M. Cernak, T. Hoder, and Z. Bonaventura, "Streamer breakdown: cathode spot formation, Trichel pulses and cathode-sheath instabilities," Plasma Sources Sci. Technol. **29**, 013001 (2020).